Additive Manufacturing: Metallurgy, Cut Analysis & Porosity

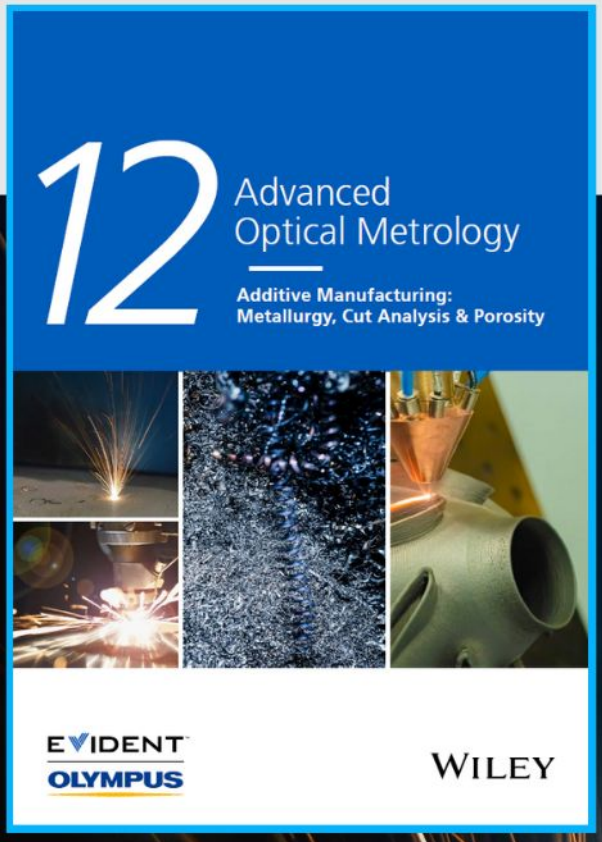

The latest eBook from Advanced Optical Metrology. Download for free.

In industry, sector after sector is moving away from conventional production methods to additive manufacturing, a technology that has been recommended for substantial research investment.

Download the latest eBook to read about the applications, trends, opportunities, and challenges around this process, and how it has been adapted to different industrial sectors.

EVIDENT
OLYMPUS

WILEY

ADVANCED FUNCTIONAL MATERIALS
www.afm-journal.de

Hierarchically Designed Super-Elastic Metafabric for Thermal-Wet Comfortable and Antibacterial Epidermal Electrode

Jiancheng Dong, Yidong Peng, Xiaolin Nie, Le Li, Chao Zhang, Feili Lai, Guanjie He, Piming Ma, Qufu Wei, Yunpeng Huang, and Tianxi Liu**

On-skin electronic systems represent a burgeoning technology that develops wearable devices capable of adapting to the dynamic surfaces of the human body. Present film-based electronics are constrained to single-layered constructions on impermeable substrates that severely inhibit their wearing comfort and multi-functionality. Herein, a thermal-wet comfortable and antibacterial epidermal electrode is hierarchically designed on an ultra-stretchable metafabric. Via the layer-by-layer assembly of trilayered elastomeric fibers with multi-scale sizes and varied compositions, porosity and wettability asymmetries are established across the nonwoven fabric, rendering it with unidirectional liquid conduction and sweat self-pumping performance. The successful printing of stretchable liquid-metal (EGaIn) circuits on ZnO NPs anchored microfibers simultaneously equips the trilayered metafabric with robust antibacterial capability, low-watt heating ability, and high-fidelity detectability for surface electromyography signals of various physical activities. Moreover, the incorporation of thermochromic microcapsules in the outmost fibers also enables the fabric Joule heater with visual indicating ability via reversible color-switching. Thus, this hierarchically engineered epidermal electrode with thermal-wet comfort and antibacterial ability holds great promise in daily applicable healthcare and sports monitoring electronics.

1. Introduction

Wearable and skin-attachable electronics with skin-like modulus, high elasticity, and diversified functionalities including breathability, thermal regulation capability, antibacterial property, and detectability for multiple physiological signals, have captured enormous research and industrial interests in the fields of medical devices, consumer electronics, and human-machine interactions (HMIs).[1] Conventional electronic devices are typically implemented in rigid or single-layer configurations, which are greatly hindered by insufficient flexibility and limited functional complexity.[2] Although it is possible to integrate the multifunctions by combining all functional components into one chip, the finite surface area of the device will be the bottleneck to its flexibility and wearing comfort.[3] An alternative approach is to assemble different chips in a multilayered configuration, thereby creating the 3D arranged electronics without affecting the modulus of the flexible matrix.[4] For example, a four-layered wearing electronic with circuits of strain and temperature sensing, wireless signal transmission, and electrophysiological detection were embedded in a stretchable silicone elastomer, achieving a compact multi-channel sensor that can be used to extract an array of signals from the human body in wireless operation mode.[5] Another research applied a layer-by-layer strategy to fabricate a stretchable multilayered electronic tattoo integrating a Joule heater and fifteen strain sensors, which further extended the development of stacking electronics.[6] Despite the above advances, most wearable electronics nowadays are fabricated using impermeable elastic thin films, the long-term wearing of which would cause serious health issues and device failures.[7] Moreover, in many health-monitoring applications, moisture or sweat permeability to analytes is critical to ensure rapid, sensitive, and accurate detection of physiological signals.[8]

In comparison with frequently used hermetical polydimethylsiloxane (PDMS) films, flexible fibrous matrixes consisting of micro/nanofibers have the advantages of intrinsically high

J. Dong, Y. Peng, L. Li, P. Ma, Y. Huang, T. Liu
Key Laboratory of Synthetic and Biological Colloids
Ministry of Education, School of Chemical and Material Engineering
Jiangnan University
Wuxi 214122, China
E-mail: hypjnu@jiangnan.edu.cn; txliu@jiangnan.edu.cn

X. Nie, Q. Wei
Key Laboratory of Eco-Textiles, Ministry of Education
Jiangnan University
Wuxi 214122, China

C. Zhang
State Key Laboratory for Modification of Chemical Fibers and Polymer Materials, College of Materials Science and Engineering
Donghua University
Shanghai 201620, China

F. Lai
Department of Chemistry
KU Leuven
Celestijnenlaan 200F, 3001 Leuven, Belgium

G. He
Christopher Ingold Laboratory, Department of Chemistry
University College London
20 Gordon Street, London WC1H 0AJ, UK

The ORCID identification number(s) for the author(s) of this article can be found under https://doi.org/10.1002/adfm.202209762.

DOI: 10.1002/adfm.202209762

permeability and high surface area, making them ideal candidates for fabricating high-performance wearable electronics.[9] Recently, permeable and stretchable three-dimensionally stacked electronics based on electrospun elastomeric fibrous mats were reported. For example, liquid metal was layer-by-layer printed onto multilayered electromyography (TPU) fiber membranes to fabricate flexible circuits, resistors, capacitors, and inductors.[10] Monolithic stretchable stacking electronics were also developed through coating liquid metal onto SBS microfibers followed by mechanical activation.[11] Apart from these, various elastomeric materials such as natural rubber, ethylene-vinyl acetate, and fluorine rubber also have been employed, amongst, the hydrogenated styrene block copolymer elastomers are regarded as the ideal candidates for skin-attachable electronics due to their excellent elasticity, resilience, and eco-friendliness.[12] In terms of conducting materials for elastic substrates, gallium-based liquid metal emerges as the most promising material for flexible electronics ascribing to its unrivaled properties including super-high electrical conductivity, theoretically unlimited ductility, excellent chemical inertness, and superior biological safety.[13] However, it is a major challenge for the uniform and stable deposition of liquid metal onto most of the elastomeric substrates because of its great surface tension and the poor interfacial adhesion force between liquid metal and polymer substrates.

In this work, an ultra-stretchable, thermal-wet comfortable, and antibacterial epidermal electrode was rationally developed based on a hierarchically engineered dual-gradient metafabric. Superhydrophobic Styrene-Ethylene-Butylene-Styrene (SEBS) and SEBS/PPO-PEO-PPO (F127) were successively processed into a bilayered nonwoven fabric with different fiber diameters, then broad-spectrum antibacterial ZnO NPs were firmly anchored onto the fibers via coupling reaction to improve the surface roughness, thus realize the successful printing of liquid metal (LM) circuits on both sides of the bilayered elastic membrane to endow the fabric with sensing and Joule heating capabilities, and simultaneously empower the fabric with stable antibacterial performance. Highly hydrophilic SEBS/TMs fibers were eventually air-blown onto the SEBS/F127 side as the outmost thermochromic layer, obtained dual-gradients of wettability and porosity across the thickness was highly beneficial for the antigravity and directional water transport. Prepared metafabric was applied as a skin-attachable and antibacterial epidermal electrode for continuous and long-term personal health management, including moisture wicking, visualized Joule heating, and human motion/biopotential monitoring under complex scenarios. Furthermore, this nonwoven bioelectrode was effectively integrated with a sEMG sensor to build advanced HMIs to control home appliances. Apparently, the thermal-wet comfortable and antibacterial metafabric in this work could be an all-around epidermal electronic system featuring high integration density, multifunctionality, and long-term wearability.

2. Results and Discussion

2.1. Design of Thermal-Wet Comfortable and Antibacterial Metafabric Electrode

Several key factors must be fulfilled for on-skin electronics to achieve stable and accurate operation and long-term wearing comfort. First, low hardness and high elasticity are fundamental to forming a conformal contact with the non-flat skin, thus allowing the intimate coupling between sensory modules and signal sources. Second, stable electrical conductivity under complex deformations (stretching, bending, twisting, etc.) is indispensable to assure the reliable acquisition of various biomechanical/bioelectrical signals under practical scenarios. Last but not least, the microenvironment of human skin can be inevitably influenced during lengthy contact with on-skin devices, potentially leading to perspiration accumulation, skin temperature anomaly, bacterial infection, and inflammation. Thus, thermal and moisture regulating ability and antimicrobial characteristics are also crucially required. In this work, hydrogenated triblock copolymer SEBS nonwoven fibrous substrates with superior stretchability, desirable softness, and great air permeability were engineered into a hierarchical trilayered structure with a dual-gradient of porosity and wettability for unidirectional sweat transportation. Besides, infinitely deformable liquid metal was stencil printed on the highly stretchable SEBS matrix to achieve Joule heating and sensing capabilities under the surface roughening of ZnO NPs, which also endow the fabric with broad-spectrum antibacterial performance. Additionally, highly-sensitive thermochromic microcapsules were embedded into the outmost air-blown microfibers as a visual-alerting indicator to avoid high skin temperature. Above designing rationales collaboratively resulting in the thermal-wet comfortable and antibacterial metafabric for an advanced epidermal electrode.

The whole fabrication process is depicted in **Figure 1**. **Figure 2**a presents a large-sized trilayered nonwoven metafabric in 30 cm × 30 cm × 300 μm, its typical cross-sectional morphology is shown in Figure 2b. It can be observed that the LM is evenly coated on the bottom side of the SEBS sub-layer, and the interface between the top (SEBS/TMs) and middle (SEBS/F127) layers (Figure 2c). The diameter and pore size distribution diagrams of each sub-layer were plotted in Figure 2d, the fiber diameters of the top, middle, and bottom layers gradually decrease from 20.74 to 1.75 μm, resulting in the decreased pore size from 76.7 to 13.6 μm. What is more, the blending of F127 and TMs greatly improves the water affinity of SEBS fibers (inset of Figure 2d), resulting in the asymmetric wettability in trilayered metafabric. Above porosity-wettability dual-gradient is highly beneficial for directional sweat transportation.[14] Pristine electrospun SEBS microfibers show smooth and transparent morphology under microscope observation (Figure 2e; Figure S4, Supporting Information), the fiber diameter significantly reduced to ≈7.5 μm after 25 wt.% addition of F127 (Figure 2d), facilitating the construction of multiscale capillary channels in the multi-layered fabric. Besides, 3D reconstruction of SEBS nonwoven in Figure 2e shows its well-defined permeable characteristics with interconnected porous structures. Since the organic matters in sweat like lactate and urea can induce bacterial proliferation, broad-spectrum antibacterial agents ZnO nanoparticles were anchored on the SEBS-SEBS/F127 bilayered nonwoven under the help of tetrabutyl titanate (TT) through a coupling reaction (Figure S5, Supporting Information),[15] where TT was applied as the linking agent between ZnO and the elastomeric microfibers. Figure 2f shows the dense and uniform coverage of ZnO NPs on the fibers (take SEBS

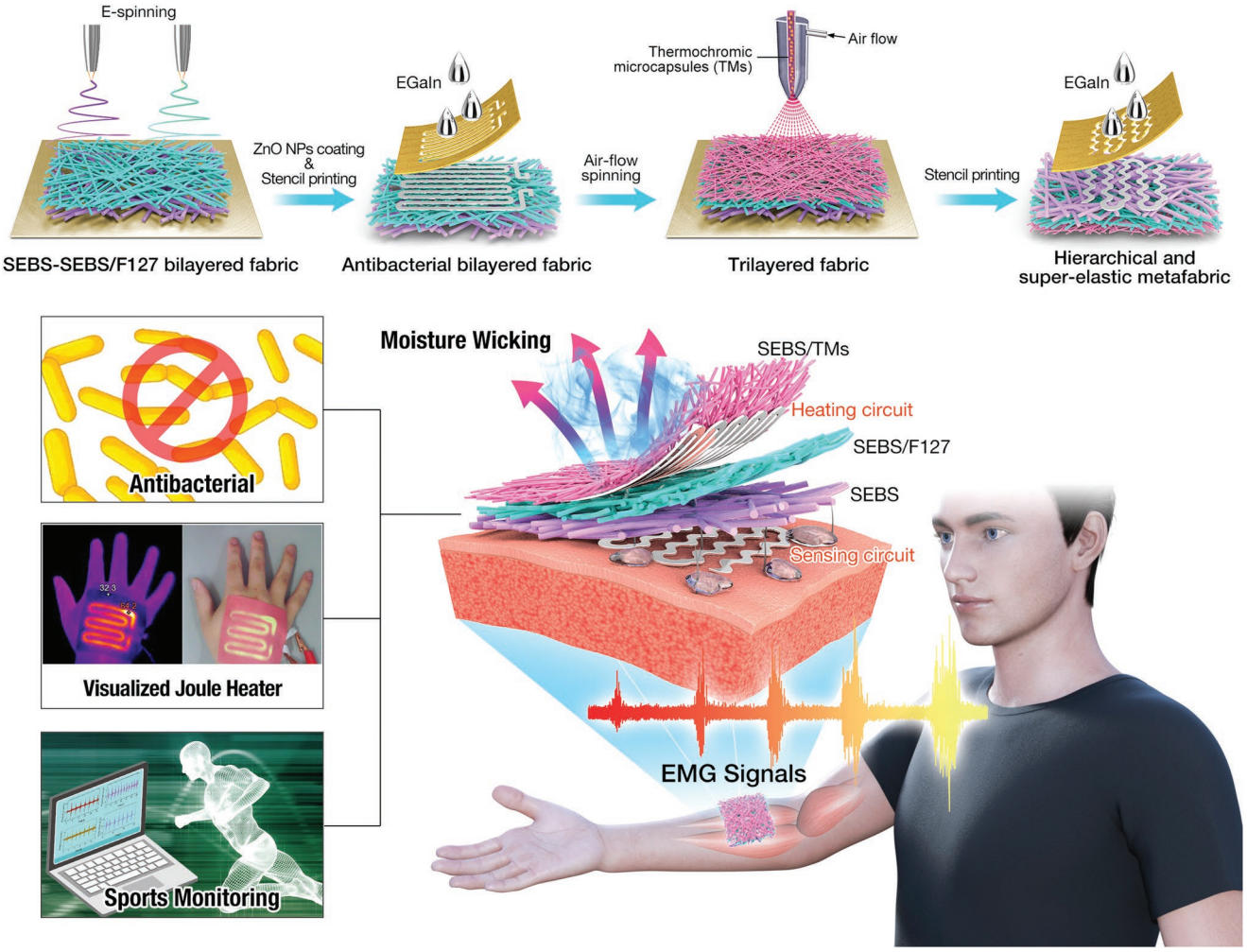

Figure 1. Schematic illustrating the fabrication of liquid metal printed hierarchical metafabrics with perspiration-wicking, visualized Joule heating, and antibacterial capabilities for advanced epidermal electrodes.

as an example), from which no obvious agglomeration and blockage can be observed. The 3D contour map of the ZnO treated fibers indicates that the fabric surface is rougher than that of pristine SEBS nonwoven, yet the excellent porosity is well retained (Figure 2f). Furthermore, Figure S6 (Supporting Information) indicates that the XRD pattern of SEBS/ZnO fibers reveals the sharp peaks of ZnO, verifying the successful incorporation of the antibacterial nanoparticles. The ZnO NPs treated nonwoven was washed for 24 and 72 h to examine its stability and fastness to washing. Figure S8 (Supporting Information) discloses that there is no obvious detachment of nanoparticles, ensuring the long-time durability of the antibacterial coating.

Liquid metal based on gallium possesses extremely high electrical conductivity (3.4×10^4 S cm^{-1}) and infinite deformability, making them perfect conducting materials for advanced electronics.[16] Nevertheless, the intrinsically high surface tension of LM (>700 mN m^{-1}) prevents its uniform and intimate incorporation with low surface energy substrates. In this research, antibacterial agent ZnO NPs on the SEBS-SEBS/F127 bilayered fabric can provide rough surfaces to improve the adhesion of LM, facilitate the printing of LM circuits on the bilayered fabric (Figure 2g). As presented in Figure 2h, a sensing circuit and a Joule heating circuit were respectively stencil printed on the SEBS side and the SEBS/F127 side of the bilayered nonwoven. The optical microscope image and SEM image further disclose that LM was uniformly deposited on the fabric, the borderline between LM and ZnO treated fabric was straight and distinct. For comparison, the LM was also printed on the untreated SEBS or SEBS/F127 nonwoven, the printing quality can be identified declining significantly from the discontinuous coverage of LM (Figure S9, Supporting Information). It is notable that low-resolution and unstable printing of LM circuits may cause a short circuit when being charged under deformation, thus potentially leading to device failure and skin injury. At last, ultra-fine SEBS fibers embedded with thermochromic microcapsules were face-to-face assembled on the Joule heating layer via air-flow spinning, thus simultaneously acting as an encapsulation layer to protect the LM circuits from external mechanical damage and chemicals. As depicted in Figure 2i–k, TMs embedded SEBS fibers present a reddish appearance, the brown thermochromic spheres (1.84 µm,

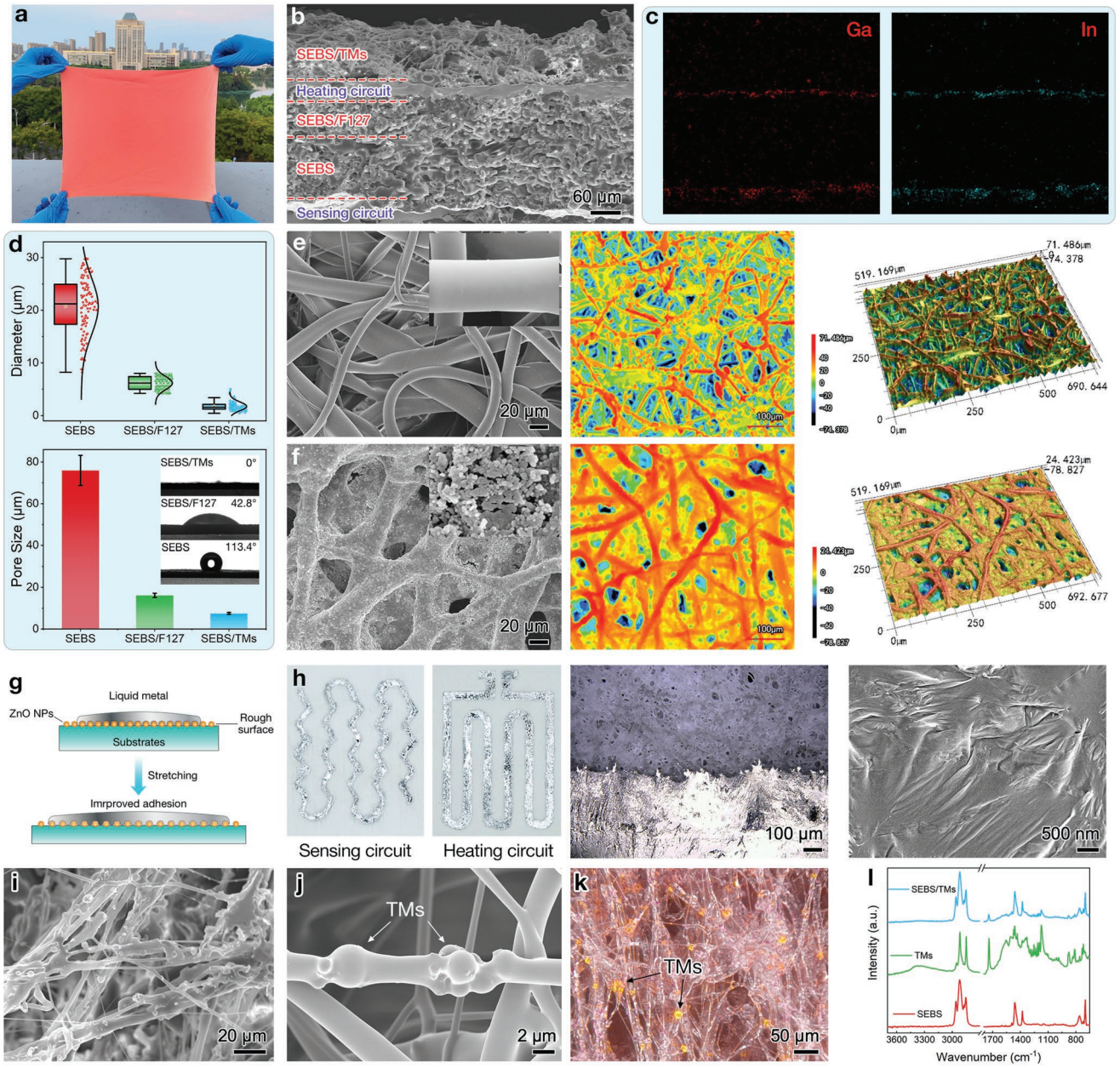

Figure 2. a) Photograph of the large-sized trilayered metafabric. b) Cross-sectional SEM image and c) corresponding elemental mapping of the metafabric. d) Diameter, and pore size distributions of each layer, inset is their corresponding water contact angles. SEM images, laser microscopic images, and 3D contour plots of e) pristine SEBS microfibers and f) ZnO NPs treated SEBS microfibers. g) Schematic depicting the improved adhesion of liquid metal on SEBS/ZnO surface. h) Digital photographs, optical microscopy, and SEM image of liquid metal printed nonwoven fabric. i,j) SEM images and k) optical microscopy of SEBS/LMs fibers. l) FTIR spectra of SEBS, TMs and SEBS/TMs microfibers.

Figure S10, Supporting Information) were partially and homogeneously embedded in the SEBS microfibers forming a necklace-like morphology. Moreover, FTIR spectrum of the thermochromic fibers shows two peaks at 3400 cm^{-1} (—OH bending) and 1750 cm^{-1} (=O bending), confirming the TMs are well combined with the elastic substrates (Figure 2l). The stable encapsulation of TM endows the metafabric with visual-alerting ability for high temperatures (>45 °C).

Reliable mechanical properties are essential for wearable electronics, which have strong impacts on the applicability and operation stability. As illustrated in **Figure 3**a,b, pure SEBS nonwoven shows relatively higher stretchability (1117.5%) and toughness (4.07 MJ m^{-3}) than that of multilayered metafabric (788.2%, 2.72 MJ m^{-3}). Nevertheless, the strength of the trilayered fabric merely decreases from 0.86 MPa (pristine SEBS) to 0.8 MPa, evidencing the excellent mechanical strength and high stretchability of the developed all-SEBS metafabric. Moreover, Young's modulus of the SEBS nonwoven increases from 46.7 to 94.4 kPa after face-to-face integration, which ideally matches the modulus of human stratum corneum (≈150 kPa).[17]

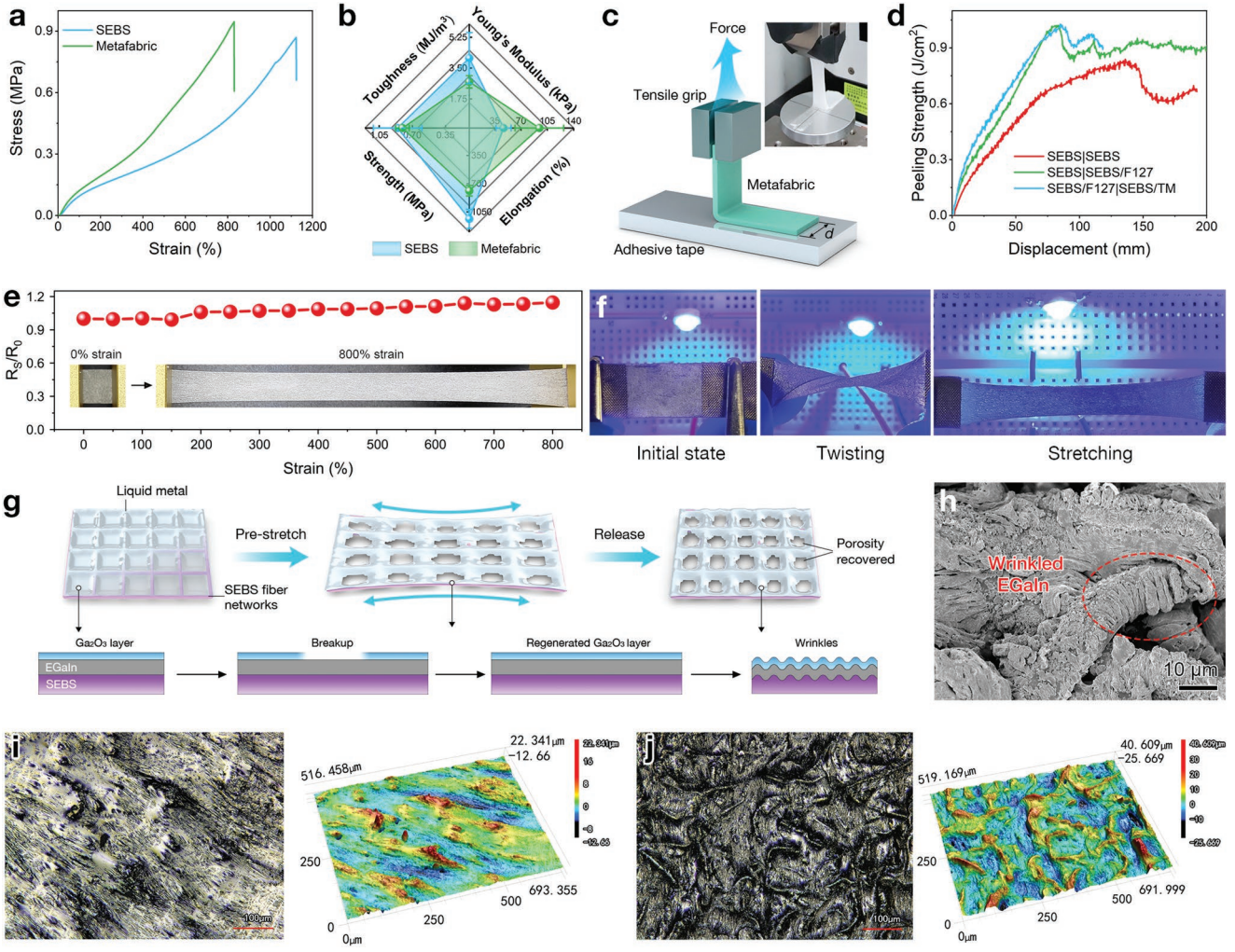

Figure 3. a) Strain–stress curves and b) the comprehensive mechanical properties of pristine SEBS and trilayered metafabric. c) Schematic illustrating the 90-degree peeling test. d) Peeling strength between different layers. e) Resistance changes of the metafabric with the strain (Insets show the metafabric at elongations of 0% and 800%). f) Metafabric applied as a super-elastic conductor to lighten an LED bulb under twisting and stretching. g) Schematic illustration describing the pre-stretching mechanism and the stable electrical conductivity of LM printed metafabric. h) SEM image of the micro-wrinkles formed during the pre-stretching process. Laser microscopic images and 3D contour plots of the LM printed metafabric i) before and j) after pre-stretching.

On-skin stretchable electronics with adequate Young's modulus are highly desirable as they can adapt to skin deformation at all times, facilitating the real-time and accurate monitoring of human physiological signals. Furthermore, the adhesive forces between the adjacent sub-layers were measured using a standard 90-degree peel testing method (Figure 3c). Thus, the adhesive force ($f = F/d$, where F is the peel force, d is the film width) is determined and plotted in Figure 3d. The peeling force between two SEBS nonwoven is measured as high as 0.81 J cm^{-2}, while the force between SEBS and SEBS/F127 is ≈1.5 times larger than bi-layered SEBS (up to 1.20 J cm^{-2}). The increased interlayer adhesion is ascribed to the dramatically increased contact sites between SEBS fibers and finer SEBS/F127 fibers. Similarly, the adhesive force between SEBS/F127 and SEBS/TM also reaches a high value of 1.09 J cm^{-2}. Thanks to the stable interface, the metafabric can readily withstand 700% stretching without detachment of sublayers (Figure S11, Supporting Information), laying a solid foundation for the mechanical stability and fatigue resistance of the trilayered metafabric.

Given the excellent stretchability and superior conductivity of printed LM circuits, the metafabric possesses stable electrical conductivity under stretching. As shown in Figure 3e, the electrical resistance increases by only 4.1% when the nonwoven was stretched to 800%. As a demonstration, one piece of trilayered metafabric applied as the wire is able to connect a circuit with an LED light under large tensile strain, bending, and twisting, when the brightness of the bulb remains unchanged (Figure 3f). The excellent and stable electrical conductivity of the metafabric mainly relies on the unique wrinkled structures of Gallium–Indium eutectic formed spontaneously on the elastic SEBS matrix during the mechanical activation process. As schematically shown in Figure 3g, a thin film of nanosized Ga_2O_3 (≈3 nm) will form instantly on the surface of bulk LM when it gets into contact with air. When the elastic substrate

is stretched, the bulk-state LM film will break up into meshes on the fiber networks, leading to the well-recovered porosity and permeability after the metafabric releases to its initial state. Meanwhile, the Ga_2O_3 layer on LM film tends to crack during large-scale stretching due to its fragile nature, which rapidly self-repairs after the new oxide layer is regenerated on the exposed LM surface. Because Ga_2O_3 is harder than the LM such that when the elastomer slowly releases to its pristine state, LM will crinkle as a result of the mechanical mismatch between the harder Ga_2O_3 layer and the softer inner LM film. The presence of porosity and wrinkles were proved after the first stretching cycle (Figure 3h). The optical images and 3D contour maps of the LM printed trilayered metafabric before (Figure 3i) and after (Figure 3j) mechanical activation imply that the liquid metal has infiltrated into the fibrous matrix after stretching/releasing, thus guaranteeing the excellent and stable conductivity. Noteworthy, the wrinkled structure of LM stemmed from mechanical activation is especially favorable for sensitive strain detection.

2.2. Joule Heating and Color-Switching Properties

The Joule heating circuit was printed on the SEBS/F127 fiber layer, which was securely sealed by the ultra-fine air-blown fibers embedded with sensitive thermochromic micro-particles, thus not only integrating heat therapy function in the trilayered metafabric, but also achieving a visual indicating capability through sharp color changing. **Figure 4**a presents the typical diagram for the coupling of Joule heating and temperature indicating. When the electric current flows through the LM circuit, thermal energy is produced attributing to Joule's law ($Q = I^2 R t$, where Q is the amount of heat, I is the input electric current, R is the electrical resistance, and t is the time that current passes through the circuit). The superhigh electrical conductivity of the LM printed metafabric can deliver a quick and sensitive Joule response to direct voltage, this characteristic can be utilized to develop a low-watt and rapid-response wearable Joule heater. As shown in Figure 4b, the surface temperature of the trilayered metafabric witnesses a sharp increase to 200 °C in <10 s under a direct voltage of 0.8 V (1.41 ± 0.01 A), which is able to cool to the ambient temperature (23 °C) within 20 s after shutting down the power supply. In addition, the fabric heater can readily rise to 30 °C under a low voltage of 0.2 V (0.29 ± 0.01 A), and is subsequently heated to 48 °C when the voltage increases to 0.3 V (0.55 ± 0.01 A), making this fabric-based Joule heater particularly useful for thermal therapy toward human joints.[18] Notably, the heating device based on liquid metal merely consumes a low power of 0.165 W, which is

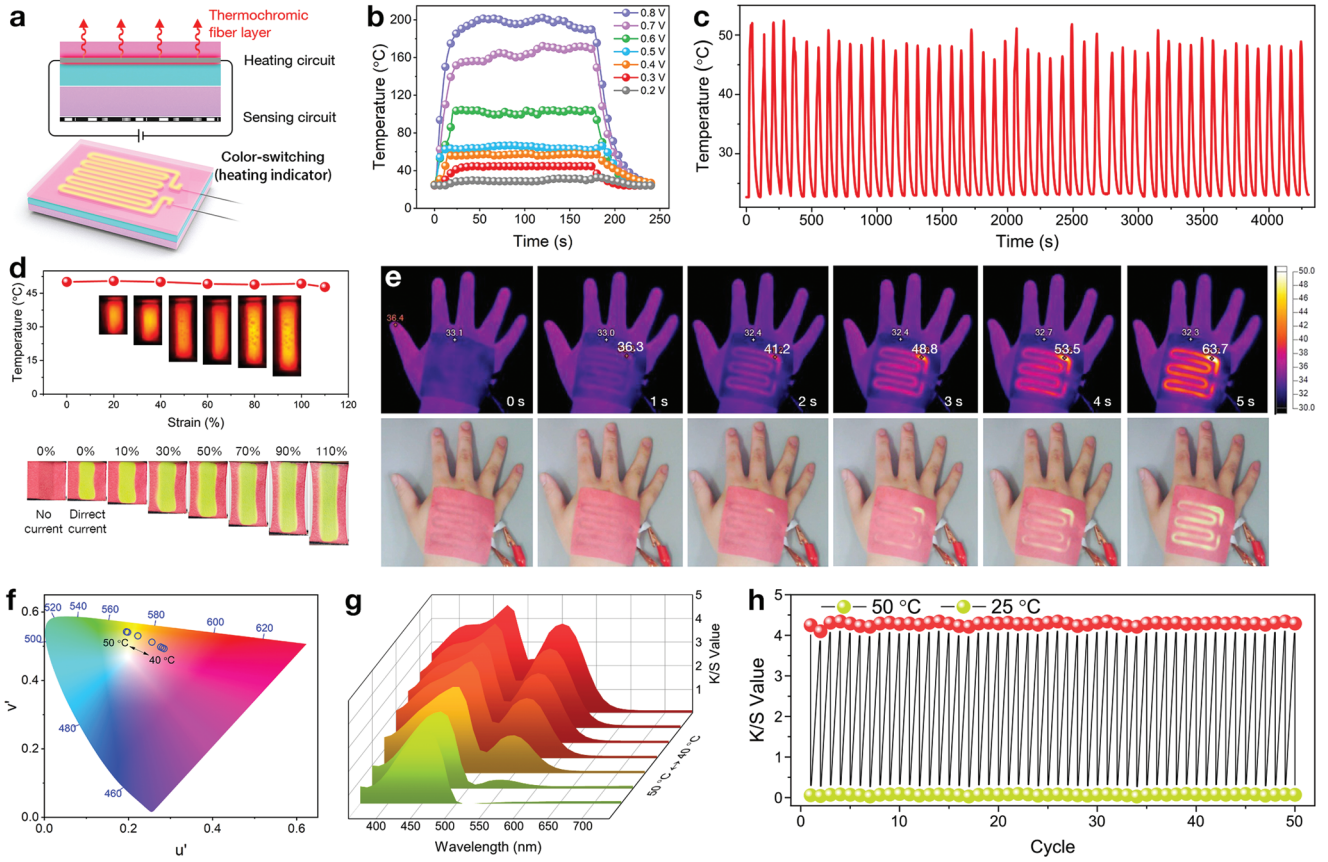

Figure 4. a) Schematic showing the structure of the visualized Joule heater in the metafabric. b) Surface temperature changes of the metafabric under varied voltages. c) Cyclic electrical heating performance of the metafabric at 0.2 V for 50 cycles. d) Surface temperatures and corresponding digital/IR images of the visualized Joule heater under different stretching strains (driving voltage of 0.2 V). e) Temperature and color changes of the visualized Joule heater at different time points (attached to the hand of a volunteer) at 0.2 V. f) CIE 1976 chromaticity diagram and g) K/S spectra of the metafabric during the thermochromic process. h) The thermochromic reversibility of the metafabric in a temperature range of 25–55 °C at 550 nm.

much more efficient than recently reported carbonaceous Joule heaters.[19] Moreover, prepared Joule heater is able to sustain consecutive power on and power off for 50 cycles with instant and stable heat response (Figure 4c), showing great stability and durability to satisfy its practical applications.

Furthermore, the surface temperature of the metafabric heater slightly changed by only 5.7% when it is gradually stretched to 110% strain (Figure 4d), indicating the excellent stability of LM circuit. Meanwhile, embedded microcapsules with a response temperature of 45 °C can be an ideal visual indicator for the Joule heater, which can switch its color from red to yellow-green under 110% stretching. Figure 4e shows the IR photographs and digital images of the metafabric on the hand with the varied input voltage, from which a well-defined circuit shape can be identified. More interestingly, there's no evident color change on the fabric when the Joule heating temperature is below 45 °C. Whereas the red color of the trilayered metafabric gradually switches to yellow-green when the temperature continuous rise beyond 45 °C. The sensitive and accurate thermochromic property of the metafabric provides a versatile and intuitive way for safe thermal therapy. The color-changing behavior of the metafabric during the thermochromic process is also reflected by the CIE 1976 chromaticity diagram (Figure 4f). Additionally, optical micrographs of the thermochromic fibers were also captured to record the color-switching process, presenting the uniform and sharp color changes at different temperatures (Figure S12, Supporting Information). The changes in the color depth during the thermochromic process can be characterized by the K/S value proposed by Kubelka and Munk in Equation 1.[20]

$$\frac{K}{S}=\frac{[1-0.01R]^2}{2[0.01R]} \tag{1}$$

where K is the absorption coefficient, S is the scattering coefficient, and R is the reflectance of the material. As shown in Figure 4g, there are two major absorption peaks located at 470 and 550 nm at room temperature (23 °C, no current input), the K/S values of the two absorption peaks significantly decrease when the temperature rises from 40 to 50 °C, especially for the peak at 550 nm (from 3.796 to 0.055). During the heating process, the crystalline violet lactone (CVL) in TM absorbs thermal energy and causes the opening of the lactone ring (colorless state), and vice versa.[21] Finally, the K/S value at 550 nm was utilized to examine the color-switching stability of the metafabric. As shown in Figure 4h, the heating/cooling process could be repeated 50 times without a significant change in the K/S value, demonstrating the excellent reversibility and stability of the thermochromic properties.

2.3. Moisture-Wicking and Antibacterial Performance

Favorable moisture and air permeability of on-skin electronics play a vital role in maintaining and regulating the human skin microenvironment.[22] The trilayered metafabric prepared by layer-by-layer assembly contains abundant interweaved channels to ensure superior permeability. As presented in **Figure 5**a, although the air permeability of the metafabric (89.2 mm s^{-1}) is a bit lower than those of commercially available cotton fabric (118.7 mm s^{-1}) and CoolMax fabric (129.5 mm s^{-1}), it is almost three times greater than that of frequently used elastic TPU fibrous mats (32.2 mm s^{-1}) in the literature. In sharp contrast, the air permeabilities of drop-casted SEBS film (thickness: ≈300 μm) and PDMS film (thickness: ≈200 μm), which are widely applied in stretchable electronic devices, are both close to zero. In addition, the moisture permeability of the trilayered fabric (1301 g m^{-2} day^{-1}) surpasses that of TPU fibers (1290 g m^{-2} day^{-1}), which can perfectly satisfy the mild perspiration of the human body.[11,23] By contrast, the moisture permeability of both casted SEBS and PDMS films is below 40 g m^{-2} day^{-1}. Furthermore, the air and water moisture permeability of the metafabric experienced merely slight changes after the LM circuits printing (Figure S14, Supporting Information).

The hierarchically architectured metafabric with porosity-wettability dual-gradient analogous to nature evolved blood vessels and plant transpiration, such asymmetric structure can facilitate fast and continuous water extraction from the hydrophobic side (electrospun SEBS/ZnO side) to the hydrophilic side (air-blown SEBS/TM side), giving rise to rapid evaporation of perspiration from human skin (Figure 5b).[14a,24] As displayed in Figure 5c, sweaty skin covered with the hierarchical metafabric gets dry very quickly within minutes in an ambient environment. The spreading and penetration behavior of water droplets (100 μL) on both sides of the metafabric are exhibited in Figure 5d,e. When dyed water is dropped on the SEBS/ZnO fibers, the droplets swiftly penetrate through the fabric, whereas the water mainly diffuses to form a large wet area when it contacts the SEBS/TM layer. To intuitively understand the directional water transport process from the hydrophobic side to the hydrophilic side, a simple physical model was employed to monitor the dynamic transport of artificial sweat droplets (dyed by sodium luciferin) under UVC light. As can be observed in Figure 5f, when the droplet contacts the SEBS/ZnO layer from the upward direction, the water can be pumped through the hydrophobic layer and wet the superhydrophilic layer in a very short time (≈0.5 s), and the transporting process is stable and unstoppable during continuous water supply (Video S1, Supporting Information). Conversely, when a water droplet dripped from above on the thermochromic side, it spreads on the SEBS/TM microfibers without wetting or penetrating the trilayered fabric (Figure 5g; Video S2, Supporting Information). More importantly, the all-SEBS fabric can maintain directional sweat transport capability under a large strain of 250% (Figure 5h; Video S3, Supporting Information) thanks to its ultra-elasticity and robust inter-layer bonding. The above results imply that the dual-gradient structural design in the metafabric can transport sweat unidirectionally from human skin to the ambient environment even under large-scale deformation. Typically, when water droplets start contacting with the porous metafabric, they get into the capillary channels and are affected by the Laplace pressure ($P = 4\gamma cos\theta/D$, where γ is the liquid-gas interfacial tension, θ is the contact angle on the fiber surface, and D is the pore size between fibers). This parameter determines whether the capillary force is negative or positive. Therefore, a simplified model in Figure 5i is used to explain the moisture-wicking process in the metafabric.[25] Due to the differential capillary pores and varied contact angles of three sub-layers, the Laplace

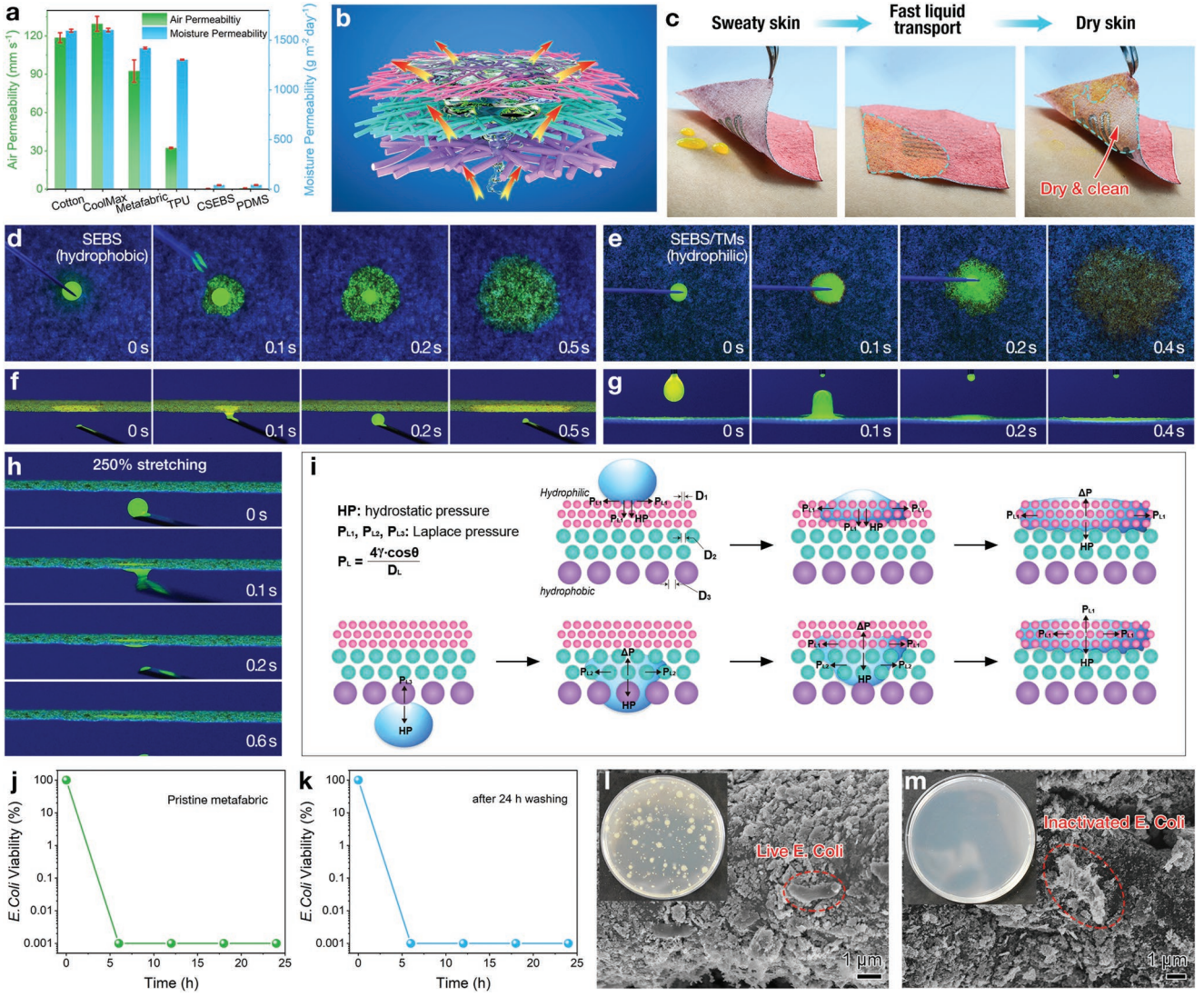

Figure 5. a) Air and water moisture permeability comparison between our nonwoven metafabric and commercial fabrics. b) Schematic depicting the unidirectional sweat transport across the trilayered dual-gradient metafabric. c) Practical application of the metafabric on fast sweat-wicking. Wetting (top view) and unidirectional liquid transport (side view) tests on the d,f) hydrophobic SEBS side (directly contact with skin), and e,g) the superhydrophilic SEBS/TMs side (thermochromic side). h) Liquid self-pumping under 250% stretching from hydrophobic side of the metafabric. i) Diagrams illustrating the simplified perspiration-wicking process in the metafabric. Antibacterial efficacy of the j) pristine metafabric and k) metafabric after 24 h washing. SEM images of l) live *E. Coli* and m) inactivated *E. Coli* on the metafabric.

pressure of liquid droplets differs in the corresponding capillary channels. Right after the liquid gets in contact with the SEBS/ZnO layer of the trilayered fabric, it will be absorbed into the pores by the capillary force. In the interface between the SEBS/ZnO layer and the SEBS/F127 layer, the sweat droplet will be subjected to two Laplace pressure P_1 and P_2 in the same direction, with the resultant sucking force in the up direction $\Delta P_1 = \frac{4\gamma\cos\theta_2}{D_2} - \frac{4\gamma\cos\theta_1}{D_1} = P_2 + |P_1|$ (where θ_1 and θ_2 are the contact angles of two layers, D_1 and D_2 represent corresponding capillary diameters). Similarly, the direction of resultant force exerts on sweat between the SEBS/F127 layer and the SEBS/TM layer is also in the upward trend, with the total value is $\Delta P_2 = P_2 + |P_3|$. Apparently, once the sweat touches the hydrophobic layer, the resulting force keeps continuously pushing the droplets upward, leading to nonreversible, directional, and even antigravity liquid transportation. Contrarily, when the sweat is dropped from above on the opposite side, it contacts the superhydrophilic fibers (SEBS/TM) and quickly spreads out due to the pulling effect of strong capillary force (CF_2) acting from all directions. After the liquid reaches the middle layer, it could permeate the hydrophilic SEBS/F127 fibers yet cannot continue to penetrate the hydrophobic SEBS fibers due to the inversed Laplace pressure, thus resulting in the sweat accumulation on the superhydrophilic side.[26] In a word, attributing to the dual-gradient structure implemented in the trilayered metafabric, sweat produced by human skin could be rapidly pumped to the outer layer with no reverse transport, thus ensuring a dry and comfortable skin environment at all times.

As the epidermal electronic device is directly attached to the human skin, the antibacterial capability is especially necessary for inhibiting microbial proliferation and ensuring cleanliness during daily wearing. Surface roughening agent ZnO NPs was utilized in this work to stabilize the LM circuit on SEBS fabric, which also acted as a broad-spectrum antibacterial agent to endow the metafabric with long-term antimicrobial performance, achieving a function of "two birds with one stone". Model bacteria Gram-negative strain *Escherichia coli* (*E. Coli*, ATCC 8739) was used to examine the antibacterial activity by the oscillation method referred to the international testing standard on a plastic surface (ISO 22196-2007, IDT).[27] Figure 5j; Figure S15, and Tables S1–S4 (Supporting Information) display the antibacterial results of prepared trilayered metafabric before and after 24 h washing. Surprisingly, ZnO NPs treated nonwoven showed superior *E. Coli* inactivation performance under incubation time of only 6 h. In the blank control group without ZnO NPs treatment, the colony units of *E. Coli* reaches 9.1×10^5 CFU cm^{-2} after 6 h culture. In contrast, the colony number in ZnO NPs incorporated fabric is no $>6.3 \times 10^{-1}$ CFU cm^{-2}, achieving an antibacterial efficacy of over 99.99%. When the incubation time increases to 12, 18, and 24 h, the metafabric also shows equivalently high antibacterial efficacy (>99.99%). Notably, ascribing to the densely and firmly incorporated ZnO NPs (Figure S8, Supporting Information), the antimicrobial performance of prepared metafabric remains intact even after 24 h intensive washing (Figure 5k), guaranteeing the robust and lengthy antibacterial performance of the metafabric. Further, the inactivation of the bacteria was investigated utilizing SEM observation. Prior to incubation, the bacteria showed rod-shaped and intact surfaces with the typical morphologies and sizes of the native cells (Figure 5l).[28] However, after incubating on the ZnO NPs grafted fabric for only 6 h, *E. Coli* strain shows remarkable signs of destructive damage featuring wrinkled and deformed shapes, corresponding to the cell membrane leakage (Figure 5m). In sharp comparison, *E. Coli* on neat SEBS nonwoven maintains the intact shapes after being incubated in PBS solution for 24 h (Figure S16, Supporting Information), showing no obvious antibacterial effects.

2.4. Monitoring of Human Physiological Signals and Human-Machine Interfaces

The trilayered metafabric printed with a stretchable and ultraconductive LM circuit is highly suitable for the detection of various forms of human physiological signals at different scales. To start with, the strain-sensing behavior of the metafabric was measured in cycles under varied tensile strains. It is found that the minimum detection strain of the sensor is as low as 0.5% (**Figure 6**a), the outputted resistance responses at both minor (0.5%–2%) and large strains (50%–300%) are stable and repeatable (Figure 6b). Moreover, the response and recovery times of the multilayered strain sensor were investigated, exhibiting a fast response of 0.6 s and a quick recovery time of 0.3 s, which can be attributed to the rapid establishment of conducting paths in the liquid metal circuit (Figure S17a, Supporting Information). Such a fast mechano-electro response enables the fabric strain sensor with point-of-care monitoring ability toward various human motions. In addition, the drifting features under static stretching of 100%, 200%, and 300% were investigated as shown in Figure S17b (Supporting Information), indicating the resistance of the strain sensor maintains extremely steady for over 300 s, evidencing the exceptional and stable conductive network in the metafabric.[29] Besides, the long-term running stability of the sensor is proved by implementing 10 000 continuous loading/unloading cycles at a fixed strain of 100% (Figure S18, Supporting Information). The fabric sensor was then attached to a volunteer's skin surface to investigate its capability for human motion monitoring. Results in Figure S17c (Supporting Information) show the sensor can readily capture the subtle motions of Adam's apple when the volunteer is swallowing and drinking. In short, the multilayered metafabric has exhibited remarkable strain sensing performances to transform different physical movements into quantifiable and instantaneous electrical signals.

The all-SEBS metafabric with low Young's modulus (94.43 kPa) possesses a comparable bending stiffness to that of human skin, guaranteeing conformal contact with the wrinkled and curved body surface.[17] Hence, the elastic and highly conductive trilayered metafabric was further applied as a skin-attachable bioelectrode to monitor an important physiological signal, namely, surface electromyography (sEMG). Figure 6c shows the bioelectrodes mounted onto the belly of the extensor digitorum (detection electrodes) and elbow joint (reference electrode), respectively, thus the sEMG signals of varied extensor contraction actions can be monitored at different gripping forces. Upon repeatedly applying a 20 kg gripping force, first increasing the gripping force and then decreasing, and applying a gradually increased gripping force of 5–25 kg, the bioelectrodes can monitor the real-timely changed sEMG signals of human muscle (Figure 6d,e). Moreover, there was no significant signal attenuation when these actions were repeated several times. Apart from these, the metafabric bioelectrode can be readily attached to the human face to collect tiny facial sEMG signals (Figure 6c). Besides, sEMG signals induced by five finger extensions can be precisely detected via attaching the fabric electrodes to the forearm (Figure 6f), the signal reliability corresponding to each finger is further confirmed by the repetition of each finger movement. Figure 6g shows three facial expressions corresponding to the typical moods human experiences in daily life (fear, laugh, and anger), where anger and laugh need more facial muscles to contract, thus resulting in stronger signal intensities. The above results reveal that the performance of the fabric bioelectrodes is comparable to other reported epidermal electrodes in the literature.[17,30] The signal-to-noise ratio (SNR) of the bioelectrode is calculated via the following formula:

$$SNR(dB) = 20 \times \log_{10} \frac{\sqrt{\sum_{k=1}^{N} V_{\text{signal}(k)}^2}}{\sqrt{\sum_{k=1}^{N} V_{\text{noise}(k)}^2}} \quad (2)$$

where N is the number of samples, $V_{\text{signal(k)}}$ and $V_{\text{noise(k)}}$ are the voltage values of the signal and noise, respectively. Thus, the SNR value for the sEMG sensor is 23.2 dB.

To further evaluate the capability of the bioelectrode in monitoring vigorous human activities, the biopotential signals of

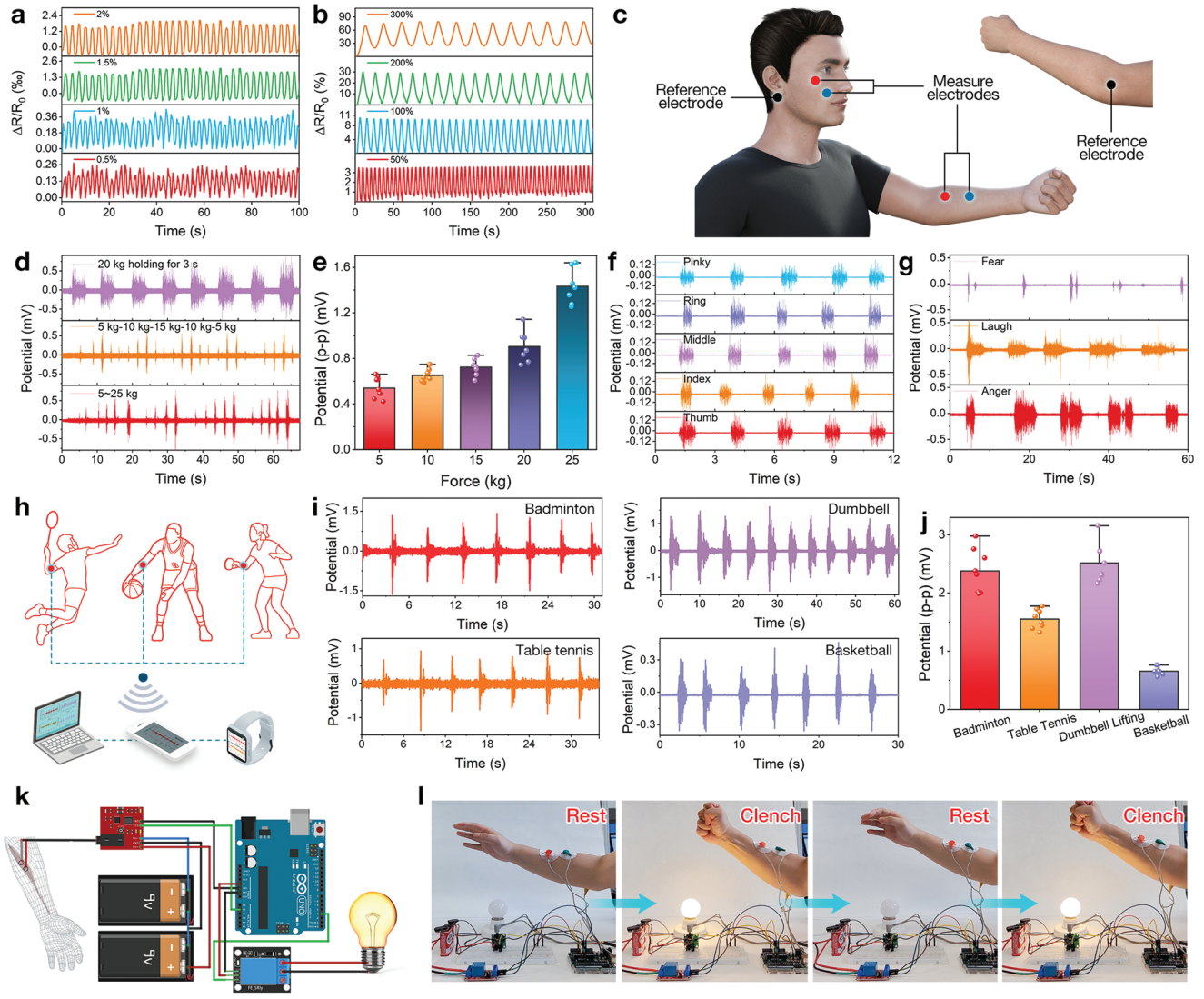

Figure 6. The strain sensing performance of the metafabric in different strain ranges of a) 0.5%≈2% and b) 50%≈300%. c) Schematic illustrating the application of our metafabric as epidermal bioelectrodes for physiological signal acquisition. sEMG signals correspond to d,e) different gripping forces, f) varied finger gestures, g) different facial expressions. h–j) Metafabric bioelectrode applied in sports monitoring based on sEMG signals: including badminton, dumbbell, table tennis, and basketball. k,l) Human-machine interface using metafabric electrode to manipulate a light bulb via fist clenching.

the human body while performing four strenuous exercises, including badminton racket swinging, table-tennis paddle swinging, dumbbell lifting, and basketball bouncing, were recorded using the metafabric as sEMG sensors (Figure 6h). As shown in Figure 6i,j, the bioelectrode can instantly generate well-defined sEMG signals for the above four activities. Especially, distinctive and characteristic sEMG patterns corresponding to different muscle activities can be perfectly acquired and displayed. For instance, the sEMG potentials of fast racket swinging and dumbbell lifting are much stronger than those of the other sports, indicating more excited muscle activities. Thus, the thermal-wet comfortable and antibacterial metafabric provides a promising alternative for sports management and athletes' training. Since the electrophysiological signals show significant applications in human-machine interface (HMIs), the sEMG signals of wrist flexors acquired by the trilayered metafabric were utilized as a user interface to control home appliances. Figure 6k depicts the simplified schematic setup and process flow for manipulating a light bulb. The sEMG signals collected by the fabric bioelectrodes are initially filtered and amplified by the signal processing unit and then supplied to the Arduino microcontroller unit to manipulate the bulb. Figure 6l and Video S4 (Supporting Information) show that when the forearm muscle contracts and loosened under the fist-clenching and resting, the light bulb can be instantly lighted and cut with no delay. Thus, the metafabric also offers a promising and alternative way for HMIs and intelligent homes. All tests on human skin were approved by the Ethics Committee of Affiliated Hospital of Jiangnan University (approval number: LS20220714).

3. Conclusion

In summary, a hierarchically structured super-elastic metafabric with diverse functionalities including antibacterial property, moisture-wicking ability, thermochromic capability, and electrical conductivity, was successfully fabricated, which could be applied as a thermal-wet comfortable epidermal electrode for long-term human bio-signal monitoring as well as human-machine interfaces. By installing the porosity and wettability gradients across the metafabric, as-fabricated trilayered bioelectrode possesses superior directional sweat transport capability. Meanwhile, the antibacterial nanoparticles closely anchored on the elastomeric fibers simultaneously ensure healthy dressing in a sweaty environment and the firm incorporation of liquid metal on the substrates. Joule heating and biosignal-sensing liquid-metal circuits in separate layers equip the metafabric with excellent thermal therapy and prominent personal health management performance. The thermochromic external layer further enables the on-skin device with visual alerting capability for heating temperature. This research offers a promising alternative for smart on-skin bioelectronics in sports management, medical devices, and artificial intelligence.

Supporting Information

Supporting Information is available from the Wiley Online Library or from the author.

Acknowledgements

This work was financially supported by the National Natural Science Foundation of China (21875033), the China Postdoctoral Science Foundation (2022M711355), the Natural Science Foundation of Jiangsu Province (BK20221540), the Shanghai Scientific and Technological Innovation Project (18JC1410600), the Program of the Shanghai Academic Research Leader (17XD1400100), the State Key Laboratory for Modification of Chemical Fibers and Polymer Materials, Donghua University, and the Postgraduate Research & Practice Innovation Program of Jiangsu Province (KYCX22_2317).

Conflict of Interest

The authors declare no conflict of interest.

Data Availability Statement

Research data are not shared.

Keywords

antibacterial, elastic metafabrics, epidermal electrodes, liquid metals, moisture wicking

Received: August 23, 2022
Revised: September 14, 2022
Published online: September 30, 2022

[1] a) Y. Dai, H. Hu, M. Wang, J. Xu, S. Wang, *Nat. Electron.* **2021**, *4*, 17; b) X. Tian, P. M. Lee, Y. J. Tan, T. L. Y. Wu, H. Yao, M. Zhang, Z. Li, K. A. Ng, B. C. K. Tee, J. S. Ho, *Nat. Electron.* **2019**, *2*, 243; c) J. Li, Y. Liu, L. Yuan, B. Zhang, E. S. Bishop, K. Wang, J. Tang, Y.-Q. Zheng, W. Xu, S. Niu, L. Beker, T. L. Li, G. Chen, M. Diyaolu, A.-L. Thomas, V. Mottini, J. B. H. Tok, J. C. Y. Dunn, B. Cui, S. P. Paşca, Y. Cui, A. Habtezion, X. Chen, Z. Bao, *Nature* **2022**, *606*, 94; d) M. Han, L. Chen, K. Aras, C. Liang, X. Chen, H. Zhao, K. Li, N. R. Faye, B. Sun, J.-H. Kim, W. Bai, Q. Yang, Y. Ma, W. Lu, E. Song, J. M. Baek, Y. Lee, C. Liu, J. B. Model, G. Yang, R. Ghaffari, Y. Huang, I. R. Efimov, J. A. Rogers, *Nat. Biomed. Eng.* **2020**, *4*, 997; e) Y. Ren, Z. Liu, G. Jin, M. Yang, Y. Shao, W. Li, Y. Wu, L. Liu, F. Yan, *Adv. Mater.* **2021**, *33*, 2008486.

[2] J. A. Rogers, T. Someya, Y. Huang, *Science* **2010**, *327*, 1603.

[3] a) Y. Zhang, H. Fu, S. Xu, J. A. Fan, K.-C. Hwang, J. Jiang, J. A. Rogers, Y. Huang, *J Mech Phys Solids* **2014**, *72*, 115; b) H. An, T. Habib, S. Shah, H. Gao, M. Radovic, J. Green Micah, L. Lutkenhaus Jodie, *Sci. Adv.* **2018**, *4*, eaaq0118.

[4] a) S. Liu, D. S. Shah, R. Kramer-Bottiglio, *Nat. Mater.* **2021**, *20*, 851; b) D. C. Kim, H. Yun, J. Kim, H. Seung, W. S. Yu, J. H. Koo, J. Yang, J. H. Kim, T. Hyeon, D.-H. Kim, *Nat. Electron.* **2021**, *4*, 671.

[5] Z. Huang, Y. Hao, Y. Li, H. Hu, C. Wang, A. Nomoto, T. Pan, Y. Gu, Y. Chen, T. Zhang, W. Li, Y. Lei, N. Kim, C. Wang, L. Zhang, J. W. Ward, A. Maralani, X. Li, M. F. Durstock, A. Pisano, Y. Lin, S. Xu, *Nat. Electron.* **2018**, *1*, 473.

[6] L. Tang, J. Shang, X. Jiang, *Sci. Adv.* **2021**, *7*, eabe3778.

[7] a) X. Yang, S. Wang, M. Liu, L. Li, Y. Zhao, Y. Wang, Y. Bai, Q. Lu, Z. Xiong, S. Feng, T. Zhang, *Small* **2022**, *18*, 2106477; b) Y. Wang, S. Lee, H. Wang, Z. Jiang, Y. Jimbo, C. Wang, B. Wang, J. J. Kim, M. Koizumi, T. Yokota, T. Someya, *Proc Natl Acad Sci USA* **2021**, *118*, e2111904118; c) K. Chang, M. Guo, L. Pu, J. Dong, L. Li, P. Ma, Y. Huang, T. Liu, *Chem. Eng. J.* **2023**, *451*, 138578; d) W. Li, S. Zheng, X. Zou, Y. Ren, Z. Liu, W. Peng, X. Wang, D. Liu, Z. Shen, Y. Hu, J. Guo, Z. Sun, F. Yan, *Adv. Funct. Mater.* **2022**, *n/a*, 2207348.

[8] a) Y. Liu, X. Huang, J. Zhou, C. K. Yiu, Z. Song, W. Huang, S. K. Nejad, H. Li, T. H. Wong, K. Yao, L. Zhao, W. Yoo, W. Park, J. Li, Y. Huang, H. R. Lam, E. Song, X. Guo, Y. Wang, Z. Dai, L. Chang, W. J. Li, Z. Xie, X. Yu, *Adv. Sci.* **2022**, *9*, 2104635; b) L. Pu, H. Ma, J. Dong, C. Zhang, F. Lai, G. He, P. Ma, W. Dong, Y. Huang, T. Liu, *Nano Lett.* **2022**, *22*, 4560; c) K. Chang, L. Li, C. Zhang, P. Ma, W. Dong, Y. Huang, T. Liu, *Composites, Part A* **2021**, *151*, 106671; d) Y. Xu, Y. Ding, L. Zhang, X. Zhang, *Compos. Commun.* **2021**, *25*, 100687.

[9] a) A. Anstey, E. Chang, E. S. Kim, A. Rizvi, A. R. Kakroodi, C. B. Park, P. C. Lee, *Prog. Polym. Sci.* **2021**, *113*, 101346; b) C. Jia, L. Li, J. Song, Z. Li, H. Wu, *Acc Mater Res* **2021**, *2*, 432; c) L. Pu, Y. Liu, L. Li, C. Zhang, P. Ma, W. Dong, Y. Huang, T. Liu, *ACS Appl. Mater. Interfaces* **2021**, *13*, 47134; d) L. Yuan, W. Fan, X. Yang, S. Ge, C. Xia, S. Y. Foong, R. K. Liew, S. Wang, Q. Van Le, S. S. Lam, *Compos. Commun.* **2021**, *25*, 100680.

[10] M. Wang, C. Ma, P. C. Uzabakiriho, X. Chen, Z. Chen, Y. Cheng, Z. Wang, G. Zhao, *ACS Nano* **2021**, *15*, 19364.

[11] Z. Ma, Q. Huang, Q. Xu, Q. Zhuang, X. Zhao, Y. Yang, H. Qiu, Z. Yang, C. Wang, Y. Chai, Z. Zheng, *Nat. Mater.* **2021**, *20*, 859.

[12] a) M. Steube, T. Johann, R. D. Barent, A. H. E. Müller, H. Frey, *Prog. Polym. Sci.* **2021**, *124*, 101488; b) I. You, M. Kong, U. Jeong, *Acc. Chem. Res.* **2019**, *52*, 63; c) J. Zeng, W. Ma, Q. Wang, S. Yu, M. T. Innocent, H. Xiang, M. Zhu, *Compos. Commun.* **2021**, *25*, 100735.

[13] S.-Y. Tang, C. Tabor, K. Kalantar-Zadeh, M. D. Dickey, *Annu. Rev. Mater. Res.* **2021**, *51*, 381.

[14] a) K. A. McCulloh, J. S. Sperry, F. R. Adler, *Nature* **2003**, *421*, 939; b) X. Zheng, G. Shen, C. Wang, Y. Li, D. Dunphy, T. Hasan, C. J. Brinker, B.-L. Su, *Nat. Commun.* **2017**, *8*, 14921.

[15] a) J.-P. Corbet, G. Mignani, *Chem. Rev.* **2006**, *106*, 2651; b) S. M. Imani, L. Ladouceur, T. Marshall, R. Maclachlan, L. Soleymani, T. F. Didar, *ACS Nano* **2020**, *14*, 12341.
[16] M. D. Dickey, *Adv. Mater.* **2017**, *29*, 1606425.
[17] Y. Zhao, S. Zhang, T. Yu, Y. Zhang, G. Ye, H. Cui, C. He, W. Jiang, Y. Zhai, C. Lu, X. Gu, N. Liu, *Nat. Commun.* **2021**, *12*, 4880.
[18] a) S. Choi, J. Park, W. Hyun, J. Kim, J. Kim, Y. B. Lee, C. Song, H. J. Hwang, J. H. Kim, T. Hyeon, D.-H. Kim, *ACS Nano* **2015**, *9*, 6626; b) Q. Zhuang, Z. Ma, Y. Gao, Y. Zhang, S. Wang, X. Lu, H. Hu, C. Cheung, Q. Huang, Z. Zheng, *Adv. Funct. Mater.* **2021**, *31*, 2105587.
[19] a) M.-B. Wu, S. Huang, T.-Y. Liu, J. Wu, S. Agarwal, A. Greiner, Z.-K. Xu, *Adv. Funct. Mater.* **2020**, *31*, 2006806; b) X. Liang, A. Fan, Z. Li, N. Wei, W. Fan, H. Liang, H. Wang, P. Bi, S. Li, X.-E. Wu, H. Lu, Q. Hao, X. Zhang, Y. Zhang, *Adv. Funct. Mater.* **2022**, *32*, 2111121; c) A. Chhetry, S. Sharma, S. C. Barman, H. Yoon, S. Ko, C. Park, S. Yoon, H. Kim, J. Y. Park, *Adv. Funct. Mater.* **2021**, *31*, 2007661; d) H. Lu, Z. Xia, X. Zheng, Q. Mi, J. Zhang, Y. Zhou, C. Yin, J. Zhang, *Compos. Commun.* **2021**, *26*, 100786.
[20] a) A. K. Roy Choudhury, in *Principles of Colour and Appearance Measurement*, (Ed: A. K. Roy Choudhury), Woodhead Publishing, Oxford **2015**; b) L. Yang, S. J. Miklavcic, *J Opt Soc Am A* **2005**, *22*, 1866.
[21] a) W. Zhang, X. Ji, C. Zeng, K. Chen, Y. Yin, C. Wang, *J. Mater. Chem. C* **2017**, *5*, 8169; b) W. Zhang, C. Wang, K. Chen, Y. Yin, *Small* **2019**, *15*, 1903750.
[22] J. Lv, G. Thangavel, Y. Li, J. Xiong, D. Gao, J. Ciou, M. W. M. Tan, I. Aziz, S. Chen, J. Chen, X. Zhou, W. C. Poh, P. S. Lee, *Sci. Adv.* **2021**, *7*, eabg8433.
[23] F. Chen, Q. Huang, Z. Zheng, *Small Struct.* **2021**, *3*, 2100135.
[24] a) L. Yang, H. Xiao, Y. Qian, X. Zhao, X.-Y. Kong, P. Liu, W. Xin, L. Fu, L. Jiang, L. Wen, *Nat. Sustain.* **2021**, *5*, 71; b) D. Miao, X. Wang, J. Yu, B. Ding, *Adv. Funct. Mater.* **2021**, *31*, 2008705.
[25] a) S. Zheng, W. Li, Y. Ren, Z. Liu, X. Zou, Y. Hu, J. Guo, Z. Sun, F. Yan, *Adv. Mater.* **2021**, *34*, 2106570; b) D. Miao, Z. Huang, X. Wang, J. Yu, B. Ding, *Small* **2018**, *14*, 1801527.
[26] a) P. Ge, S. Wang, J. Zhang, B. Yang, *Mater. Horiz.* **2020**, *7*, 2566; b) X. He, S. Yang, Q. Pei, Y. Song, C. Liu, T. Xu, X. Zhang, *ACS Sens.* **2020**, *5*, 1548.
[27] E. Zhang, X. Zhao, J. Hu, R. Wang, S. Fu, G. Qin, *Bioact Mater* **2021**, *6*, 2569.
[28] J. Dong, R. A. Ghiladi, Q. Wang, Y. Cai, Q. Wei, *Nanotechnology* **2018**, *29*, 265601.
[29] M. N. Ren, Y. Zhou, Y. Wang, G. Q. Zheng, K. Dai, C. T. Liu, C. Y. Shen, *Chem. Eng. J.* **2019**, *360*, 762.
[30] a) L. Zhang, K. S. Kumar, H. He, C. J. Cai, X. He, H. Gao, S. Yue, C. Li, R. C.-S. Seet, H. Ren, J. Ouyang, *Nat. Commun.* **2020**, *11*, 4683; b) P. Tan, H. Wang, F. Xiao, X. Lu, W. Shang, X. Deng, H. Song, Z. Xu, J. Cao, T. Gan, B. Wang, X. Zhou, *Nat. Commun.* **2022**, *13*, 358.